

STRUCTURAL BIOLOGY

Binding mechanisms of therapeutic antibodies to human CD20

Anand Kumar^{1,2,3}, Cyril Planchais^{4,5}, Rémi Fronzes^{3,6}, Hugo Mouquet^{4,5}, Nicolas Reyes^{1,2,3*}

Monoclonal antibodies (mAbs) targeting human antigen CD20 (cluster of differentiation 20) constitute important immunotherapies for the treatment of B cell malignancies and autoimmune diseases. Type I and II therapeutic mAbs differ in B cell binding properties and cytotoxic effects, reflecting differential interaction mechanisms with CD20. Here we present 3.7- to 4.7-angstrom cryo-electron microscopy structures of full-length CD20 in complexes with prototypical type I rituximab and ofatumumab and type II obinutuzumab. The structures and binding thermodynamics demonstrate that upon binding to CD20, type II mAbs form terminal complexes that preclude recruitment of additional mAbs and complement components, whereas type I complexes act as molecular seeds to increase mAb local concentration for efficient complement activation. Among type I mAbs, ofatumumab complexes display optimal geometry for complement recruitment. The uncovered mechanisms should aid rational design of next-generation immunotherapies targeting CD20.

Human cluster of differentiation 20 (CD20) (1, 2) is an integral membrane protein expressed during B lymphocyte development (3). Its cellular function is poorly understood, and it is involved in intracellular calcium signaling associated with the B cell receptor (4). CD20 is also expressed in malignant B cells and is the target of approved therapeutic monoclonal antibodies (mAbs), which are divided into two groups, type I and type II, on the basis of two signature differences (5–8): Type I mAbs recruit complement more potently than type II mAbs and therefore induce robust complement-dependent cytotoxicity (CDC); type I mAbs bind twice as many type II mAbs to a given B cell type. These properties are likely related, because complement activation requires oligomerization of the mAb fragment crystallizable region (Fc) to increase the binding avidity of complement component 1q (C1q), which is a hexa-headed molecule that optimally binds Fc hexameric arrangements (9–11).

Type I rituximab (RTX) is a recombinant mAb bearing murine antigen-binding domains linked to human immunoglobulin G (IgG) constant domains. RTX is recommended for the treatment of non-Hodgkin's lymphomas (12) and certain autoimmune diseases (13) and was the first approved cancer immunotherapy (14). Despite the widespread use of RTX, its immunogenicity and patient polymorphisms stimulated the development of second-generation mAbs that replaced the murine domains with

humanized or human antigen-binding domains, as with the type II mAb obinutuzumab (OBZ) (15) and the type I mAb ofatumumab (OFA) (16), respectively, which are approved for the treatment of chronic lymphocytic leukemia (CLL) (8, 17). Although OFA is a type I mAb, it shows more potent complement recruitment than RTX, particularly in cells with low CD20 expression levels, as occurs in CLL (18, 19).

Binding studies (20, 21) and crystal structures of monovalent antigen-binding fragments (Fabs) of RTX (Fab_{RTX}) (22) and OBZ (Fab_{OBZ}) (23) in complex with CD20 cyclic peptides revealed a critical antigenic determinant region (¹⁷⁰ANPS¹⁷³) on the large extracellular loop of CD20, as well as 1:1 Fab:CD20 peptide binding stoichiometry (24). Recently, the cryo-electron microscopy (cryo-EM) structure determination of N-terminally truncated CD20 in complex with Fab_{RTX} (Δ 41CD20-Fab_{RTX}) showed two Fab_{RTX} molecules bound to composite epitopes on the surface of dimeric CD20 and revealed extensive Fab-Fab homotypic interactions (25).

Despite the wealth of available functional and structural data, the molecular bases underlying the differential binding mechanisms of murine versus human type I mAbs, as well as those for type I versus type II mAbs, remain elusive. We set out to unravel these mechanisms using *in vitro* approaches to determine the three-dimensional (3D) structures and binding mechanisms of full-length human CD20 in complex with Fab fragments from three major therapeutic mAbs: RTX (murine type I), OFA (human type I), and OBZ (humanized type II).

Results

Antibody binding and complement recruitment

Full-length human CD20 in nondenaturing detergent solutions exists as a single and stable oligomeric state corresponding to homodimers (fig. S1). To probe the ability of purified CD20 to

reconstitute the properties of type I and type II mAbs, we analyzed their binding thermodynamics and kinetics by using isothermal titration calorimetry (26, 27), as well as the mAbs' abilities to recruit complement.

Isothermal titrations of full-length Ig molecules bearing identical IgG1 Fc regions and corresponding Fab fragments from either RTX (IgG_{RTX}) or OBZ (IgG_{OBZ}) into purified CD20 yielded dissociation constant (K_d) values in the low nanomolar range, as observed in B cells (15), and binding stoichiometries of 1:1 and 1:2 for IgG_{RTX} and IgG_{OBZ}, respectively, providing the thermodynamic basis to understand the half-maximal values of type II compared to type I mAb binding to B cells.

Further calorimetric analysis of both divalent [F(ab')₂] and monovalent (Fab) mAb fragments from RTX, OBZ, and OFA (Fig. 1, A to D, and table S1) yielded conserved thermodynamic binding parameters, compared to full-length IgGs. Moreover, molecules bearing Fab_{RTX} showed higher binding enthalpy values (-27.4 ± 0.6 kcal/mol) than those bearing Fab_{OBZ} (-19.0 ± 0.8 kcal/mol) or Fab_{OFA} (-23.0 ± 0.8 kcal/mol), although the large excess of binding enthalpy translates to a small change in binding energy (~ 1 kcal/mol) due to entropic compensations. From a kinetic viewpoint, we observed similar association rate (k_{on}) values for the three F(ab')₂ molecules but significantly slower dissociation rates of F(ab')_{2-RTX} than for both F(ab')_{2-OBZ} and F(ab')_{2-OFA} (table S2).

We next probed the ability of IgG_{RTX} and IgG_{OBZ} bound to purified CD20 to recruit complement (Fig. 1E). As a proxy for complement recruitment, we quantified the deposition of fluorescently labeled C1q complex on synthetic liposomes with CD20 incorporated on their surface, as well as on HEK293 cells expressing CD20, as a control. Indeed, C1q deposition was much higher in both cells and liposomes opsonized with IgG_{RTX} than those opsonized with IgG_{OBZ}, demonstrating that dimeric CD20 reconstituted in a synthetic membrane is sufficient to promote Fc oligomerization and complement recruitment.

Overall, the above results demonstrate that binding of mAbs to purified dimeric CD20 recapitulates accurately the signature differences between type I and type II anti-CD20 antibodies observed in B lymphocytes.

Cryo-EM structural analysis of CD20 in complex with divalent antibody fragments

For cryo-EM structure determination, we focused on CD20 complexes with divalent F(ab')₂ molecules from RTX, OFA, and OBZ, because they structurally resemble full-length mAbs more closely than monovalent fragments and lack flexible Fc domains that might complicate single-particle reconstructions. Cryo-EM imaging showed that the majority of the CD20

¹Membrane Protein Mechanisms Unit, Institut Pasteur, 75015 Paris, France. ²Membrane Protein Mechanisms Group, European Institute of Chemistry and Biology, University of Bordeaux, 33607 Pessac, France. ³CNRS UMR 5234 Fundamental Microbiology and Pathogenicity, Bordeaux, France. ⁴Laboratory of Humoral Immunology, Department of Immunology, Institut Pasteur, Paris, France. ⁵INSERM U1222, Paris, France. ⁶Structure and Function of Bacterial Nanomachines Group, European Institute of Chemistry and Biology, University of Bordeaux, 33607 Pessac, France. *Corresponding author. Email: nicolas.reyes@u-bordeaux.fr

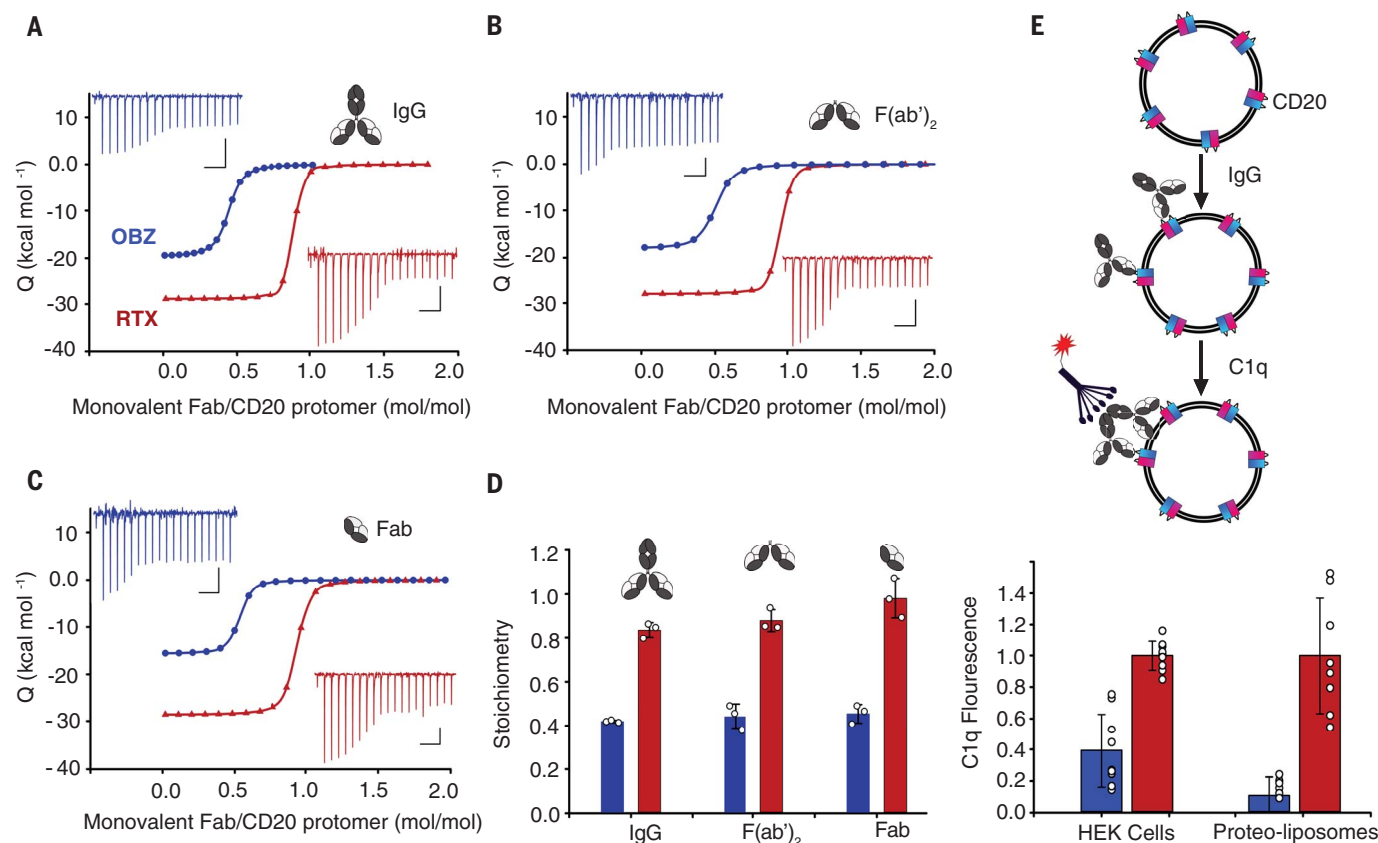


Fig. 1. Antibody binding and complement recruitment. (A to C) Isothermal titrations of IgG (A), F(ab')₂ (B), and Fab (C) molecules into purified CD20. Thermal powers are shown, with scale bars indicating 0.1 μ cal s⁻¹ and 500 s. Throughout the figure, RTX and OBZ data are colored red and blue, respectively. Q , binding heat. (D) Averaged binding stoichiometry of monovalent and divalent molecules to CD20. Stoichiometry is plotted as moles of monovalent

Fab per mole of CD20 protomer for comparison. (E) Fluorescently labeled C1q deposition upon IgG opsonization of liposomes and cells with CD20 on their surface. Plots depict an average of three independent experiment measurements (D) or three independent experiment measurements performed in triplicates (E), and error bars represent SEM. Empty circles represent values from individual experiments.

complexes with type I F(ab')₂ molecules formed 2:2 F(ab')₂:CD20 cyclic arrangements; we also observed 3:3 and 4:4 arrangements, but not 1:1 complexes (Fig. 2, A and B). In contrast, CD20 complexes with type II F(ab')₂OBZ showed exclusively 1:2 arrangements (Fig. 2C). A feature common to all of these macromolecular assemblies is that the two Fab arms from one F(ab')₂ molecule bind two CD20 molecules. However, we observed that the CD20 dimer binds two type I Fab molecules, but only one type II Fab molecule. These structural data are in excellent agreement with our thermodynamic analysis and further show that the two type I Fabs bound to CD20 come from different F(ab')₂ molecules.

The large flexibility of F(ab')₂ fragments around the hinge region connecting the Fab arms precluded high-resolution 3D reconstructions. To alleviate this problem, we decreased the particle box size to extract only one copy of CD20 from the macromolecular assemblies with either two type I (Fig. 2, D and E) or one type II (Fig. 2F) Fab molecule bound, respectively. This “single-copy approach” effectively increased the number of particles and decreased particle het-

erogeneity, and as a consequence it improved the quality of 2D classes and 3D reconstructions substantially, yielding cryo-EM maps with global resolutions between 3.7 and 4.7 Å that enabled structure determinations of CD20 in complex with Fab_{RTX}, Fab_{OFA}, and Fab_{OBZ}, respectively (figs. S2 to S7 and table S3).

Cryo-EM structures of CD20 in complexes with type I Fab

The cryo-EM structures of full-length CD20 in complexes with murine Fab_{RTX} (CD20-Fab_{RTX}) and human Fab_{OFA} (CD20-Fab_{OFA}) showed two CD20 subunits (here, CD20_A and CD20_B) arranged in a symmetric dimer with two Fab-bound molecules (Fig. 3, A to D).

Each CD20 subunit contains four trans-membrane helices (TM1 to -4) (Fig. 3E). TM1 barely spans the width of the membrane core, while TM2 unwinds close to the midpoint of the membrane, dividing the helix into TM2a and TM2b. TM1 and TM2a are connected by extracellular loop 1 (ECL1), which positions Gly⁷⁵, Ile⁷⁶, and Tyr⁷⁷ outside the membrane plane. The region including TM2b and the in-

tracellular loop that connects it to TM3 (ICL1), and also TM4, differs significantly in the CD20-Fab_{RTX} and CD20-Fab_{OFA} structures compared to the reported Δ 41CD20-Fab_{RTX} structure (25). In the former, TM2b is a canonical α helix including residues Leu⁸⁸-Ala¹⁰³, while in the latter TM2b was modeled as a 3-10 α helix between Ile⁹⁶ and Ile¹⁰¹ with an extended ICL1. Additionally, in our structures TM4 is three helix turns longer than in Δ 41CD20-Fab_{RTX} and protrudes outside the membrane plane on the intracellular side. The observed differences are most likely due to low molecular detail around those regions in the reported Δ 41CD20-Fab_{RTX} cryo-EM map (EMD-21212), or partial unfolding of the truncated construct.

TM3 and TM4 are connected by ECL2: Its N-terminal residues form an amphipathic loop (ECL2a) that partitions in the lipid-detergent micelle with hydrophobic side chains buried in the membrane core, next to extra density corresponding to lipid or detergent molecules arranged in a bilayer fashion. The C-terminal part of ECL2 (ECL2b) is flanked by two extracellular helices (EH), α helix EH1 and 3-10 α

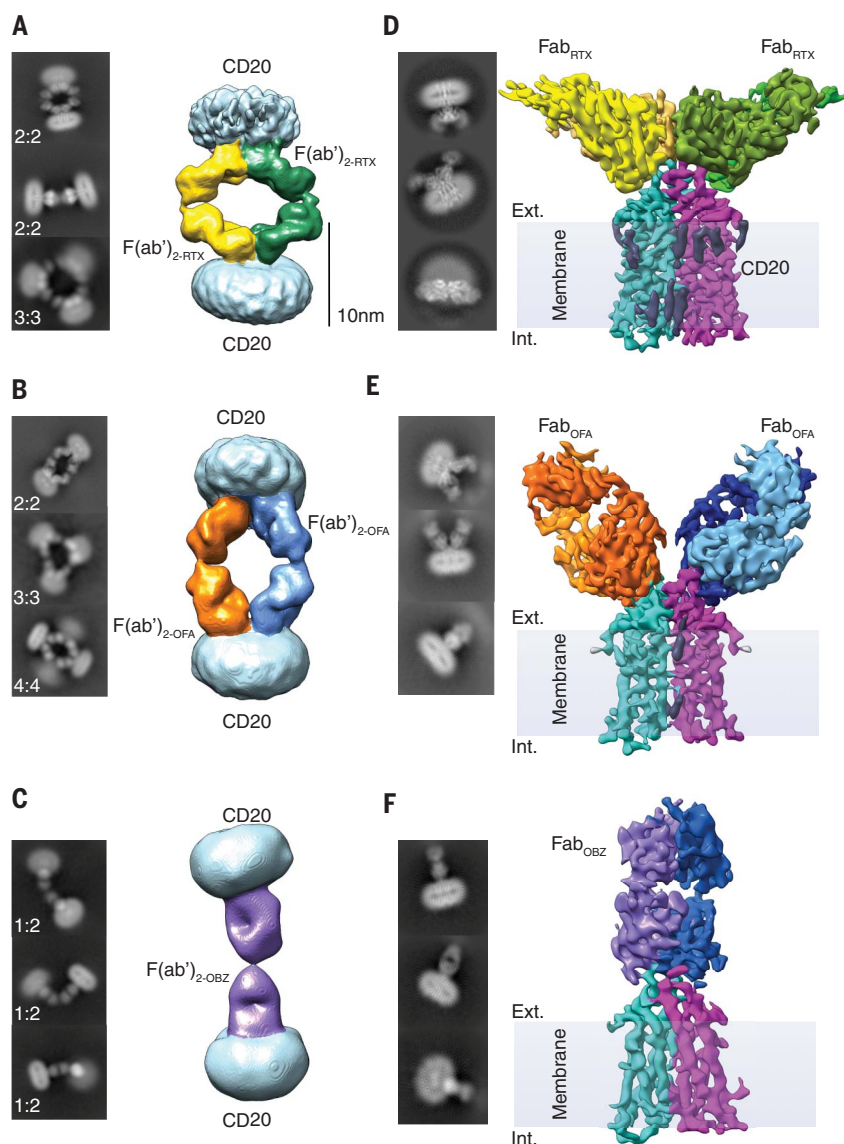


Fig. 2. Cryo-EM analysis of CD20- $F(ab')_2$ complexes. (A to C) 3D reconstructions of 2:2 $F(ab')_2$:CD20 assemblies, with lipid-detergent micelles colored light blue and individual $F(ab')_2$ molecules color coded. 2D classes are also shown for 2:2, 3:3, and 4:4 assemblies. (D to F) Cryo-EM maps of a single copy of CD20 bound to Fab (individual CD20 subunits in cyan and pink, respectively) within the CD20- $F(ab')_2$ assemblies with Fab (heavy and light chains in dark and light colors, respectively) and lipid (gray) molecules bound. Examples of 2D classes in different orientations are shown. Ext., exterior; Int., interior.

helix EH2, and is linked to TM4 through a disulfide between Cys¹⁶⁷ and Cys¹⁸⁴, which is strictly conserved among CD20 orthologs.

The two Fab-bound molecules in CD20-Fab_{RTX} and CD20-Fab_{OFA} structures are arranged head-to-head with their Fab constant domains oriented in opposite directions (Fig. 3, A and B). Notably, Fab_{OFA} binds at a sharper angle to the membrane plane ($\sim 60^\circ$) than Fab_{RTX} ($\sim 36^\circ$) and is rotated $\sim 180^\circ$ along the long axis of the Fab. As a consequence, the variable domains of the two bound Fab_{OFA} molecules separate, with their closest atoms at ~ 7 Å, and do not establish any homotypic

contacts, while the constant domains come in closer proximity by as much as ~ 9 Å, compared to RTX.

RTX and OFA bind overlapping and extensive 3D epitopes that bury ~ 890 and ~ 720 Å² on the extracellular surface of CD20, respectively (Fig. 3, C and D), mostly through amino acid interactions with their heavy-chain complementary determinant regions (HC-CDR) (table S4). However, the orientations of RTX and OFA HC-CDRs are opposite, with the former crossing the CD20 dimeric interface and establishing Fab-Fab homotypic interactions and the latter lying ~ 40 Å apart from

each other and pointing to the membrane. As a consequence, RTX interacts mainly with residues ¹⁷⁰ANPS¹⁷³ in EH2, while OFA interacts with residues Tyr¹⁶¹, Asn¹⁶⁶, and Glu¹⁶⁸ in ECL2b, as well as Ala¹⁷⁰ and Asn¹⁷¹ in the tip of CD20 (Fig. 3, C and D, and table S4). The more N-terminal location of CD20 determinant residues for OFA, in comparison with RTX binding, is in excellent agreement with reported binding studies (28).

Overall, our structural comparison showed that the OFA epitope is restricted to one CD20 subunit and its core interactions localize to ELC2b and EH2, while Fab_{RTX} recognizes both CD20 subunits and its core epitope localizes to EH2. OFA orients its Fab constant domains closer to each other than RTX while separating its variable domains that lack homotypic interactions.

RTX homotypic Fab-Fab interactions

CD20-bound Fab_{RTX} molecules establish unexpected Fab-Fab homotypic interactions (25) (fig. S8). These interactions occur at germline-encoded positions that are not the product of affinity maturation (25), raising an important question about the strength of the interactions and the extent of the thermodynamic coupling at the homotypic interface. To shed light on this problem, we built a double mutant thermodynamic cycle (29), introducing amino acid exchanges on opposite sides of the CD20-Fab_{RTX} homotypic interface, and tested if the effect on IgG_{RTX} binding of mutating residues on one side depends on whether residues on the other side are mutated. Four tyrosine residues play critical roles at this interface (fig. S8A): Tyr¹⁰¹(HC-CDR3) forms an aromatic stack with symmetry-related Tyr¹⁰¹; Tyr¹⁰²(HC-CDR3) makes contacts with Thr²⁸(HC-CDR1), Ser³¹(HC-CDR1), and Tyr³²(HC-CDR1) and is hydrogen-bonded to Thr²⁸(HC-CDR1); Tyr⁵²(HC-CDR2) and Tyr⁴⁸(LC-CDR2) are hydrogen-bonded to Gly¹⁰³(HC-CDR3) and Ser³¹(HC-CDR1), respectively. To build the cycle, we exchanged amino acid side chains to impair their ability to form H-bonds using the following IgG_{RTX} constructs (fig. S8C): (i) wild type (WT), (ii) Thr²⁸→Ala Ser³¹→Ala (T28A-S31A), (iii) Tyr¹⁰²→Phe Tyr⁴⁸→Phe (Y102F-Y48F), and (iv) T28A-S31A-Y102F-Y48F. Isothermal titrations showed that all IgG_{RTX} constructs bind CD20 with 1:1 stoichiometry and similar K_d values (fig. S8C and table S5). Notably, we observed a significant increase in favorable binding enthalpy when mutations T28A-S31A were introduced in WT IgG ($\Delta\Delta H = -5.5$ kcal/mol) compared to those mutations introduced in the background of Y102F-Y48F ($\Delta\Delta H = -0.93$ kcal/mol), showing that there is detectable thermodynamic coupling at the homotypic interface. However, the observed enthalpic changes are not translated into significant changes in IgG_{RTX} affinity due to entropic compensations,

Fig. 3. Structures of CD20 complexes with type I Fab fragments.

(A and B) Structures of CD20 in complexes with two Fab_{RTX}-bound (A) and Fab_{OFA}-bound (B) molecules, color coded as in Fig. 2, D to F. Insets show extracellular views of the Fab variable domains bound to CD20. (C and D) The most important CD20 residues interacting with single Fab_{RTX-A} (yellow; C) or Fab_{OFA-A} (orange; D) molecules are highlighted. Residues in ball-and-stick representation establish the majority of H-bonds and contacts with the Fab molecule. Single-letter abbreviations for the amino acid residues are as follows: A, Ala; C, Cys; D, Asp; E, Glu; F, Phe; G, Gly; H, His; I, Ile; K, Lys; L, Leu; M, Met; N, Asn; P, Pro; Q, Gln; R, Arg; S, Ser; T, Thr; V, Val; W, Trp; and Y, Tyr. (E) Membrane view of CD20_A subunit from the CD20-Fab_{RTX} complex.

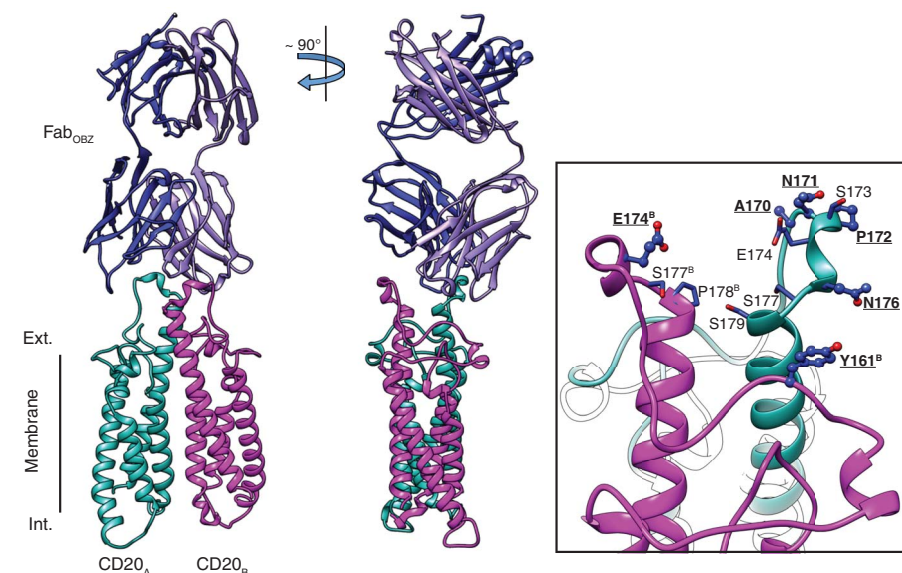
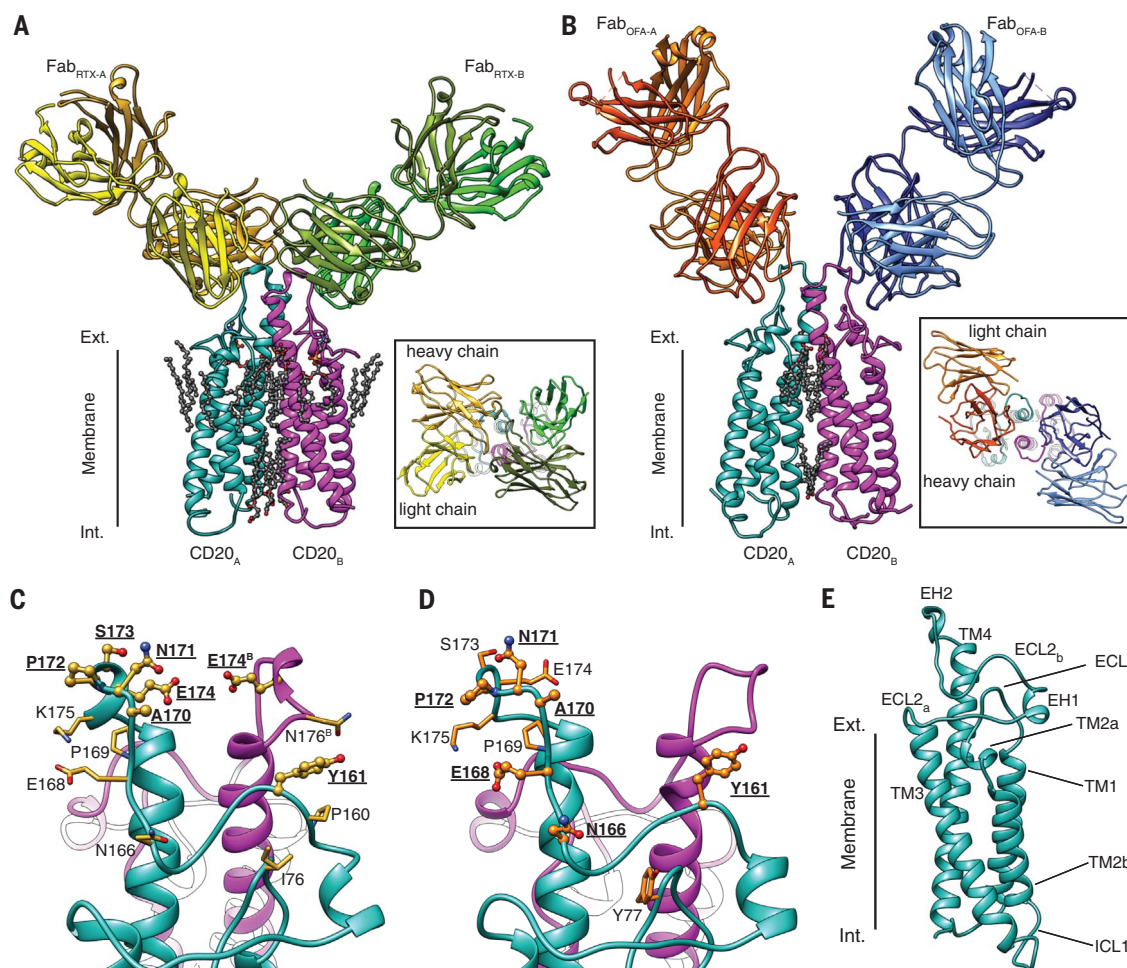


Fig. 4. Structure of CD20 in complex with type II Fab_{OBZ}. Structure of CD20 with one Fab_{OBZ}-bound molecule. Fab_{OBZ} interacts more extensively with CD20_A subunit (cyan), but it also interacts with CD20_B (pink). Inset shows the most important CD20 residues interacting with Fab_{OBZ}. Residues in ball-and-stick representation establish the majority of H-bonds and contacts with the Fab molecule.

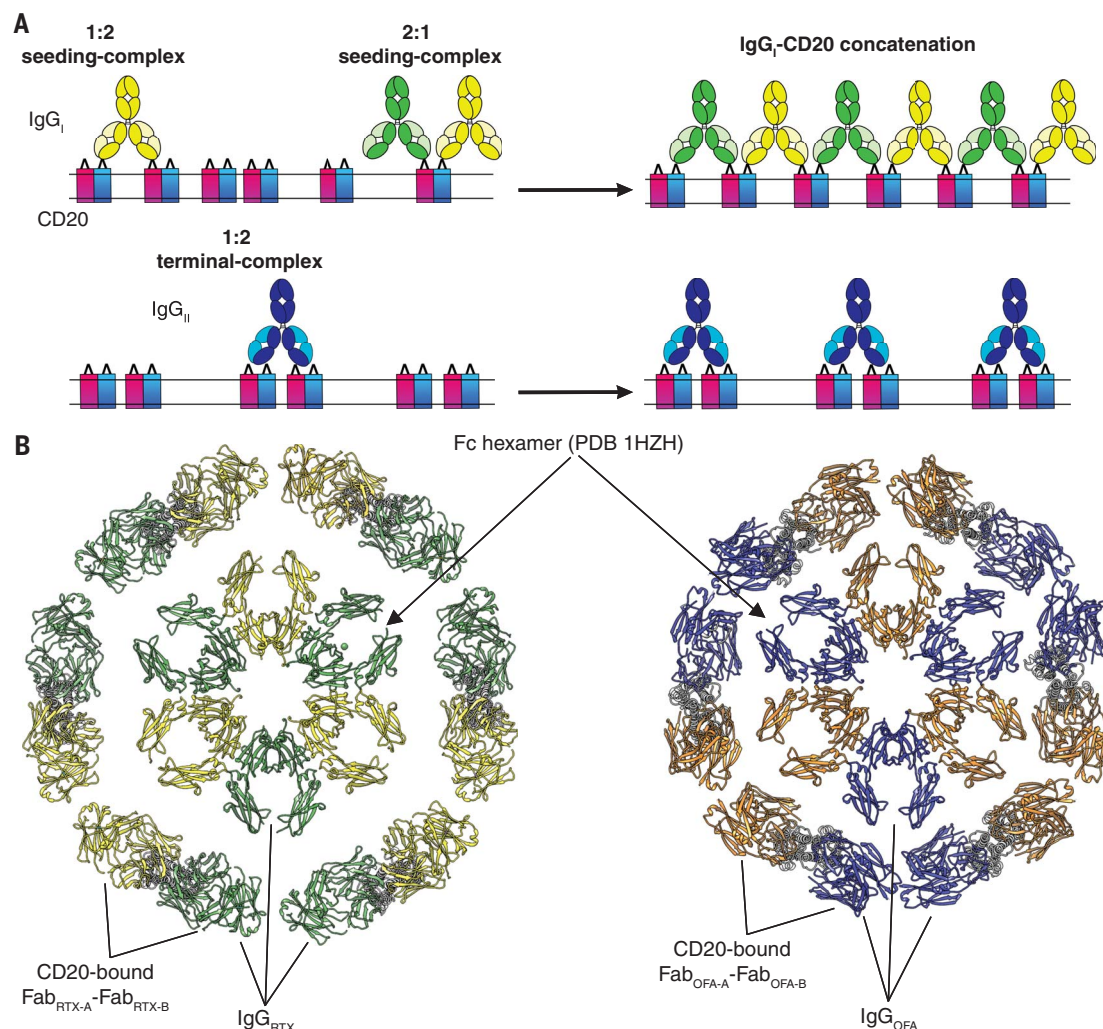
demonstrating that the H-bond network at the core of the homotypic interface contributes weakly to the overall binding energy.

CD20 complex with type II OBZ fragments

To gain insights into the differential binding mechanisms of type I and II anti-CD20 mAbs, we determined the structure of CD20 in complex with type II Fab_{OBZ} (Fig. 4). The structure showed a single Fab_{OBZ} molecule bound to the tip of CD20, with pseudosymmetric CD20 subunits in a conformation similar to those in the CD20-Fab_{RTX} structure. In contrast to type I Fab molecules, Fab_{OBZ} binds nearly normally to the membrane plane, with its constant domain protruding far into the extracellular solution.

Fab_{OBZ} forms a wide and rather shallow binding pocket involving all CDR loops, with the exception of CDR-L2, to bind extensive areas on the surface of both CD20_A (~566 Å²) and CD20_B (~226 Å²). Binding to CD20_A occurs at an extended ¹⁷⁰ANPSEKNSP¹⁷⁸ motif, with key interacting residues ¹⁷⁰ANP¹⁷² and EH2 C-terminal Glu¹⁷⁴ and Asn¹⁷⁶ residues (table S4). The C-terminal shift of the OBZ

Fig. 5. Binding mechanism and hexameric CD20-IgG model. (A) IgG:CD20 seeding and terminal complex mechanisms for type I and II mAbs, respectively. **(B)** Extracellular view of a structural model built with the symmetric Fc hexamer from PDB 1HZH and six copies of CD20-Fab_{RTX} (left) or CD20-Fab_{OFA} (right) structures (determined in this work), arranged symmetrically and concentric to the Fc ring. The space between CD20-Fab complexes was minimized to avoid clashes between Fab domains bound to different CD20 molecules. Fc domains and the two corresponding Fab domains are shown in the same color.



epitope compared to RTX is in good agreement with previous binding and structural studies (23). Other residues in CD20_A establish contacts mostly with the light chain, while heavy-chain Arg⁵²(CDR-H2) and Trp³³(CDR-H1) are H-bonded to Pro¹⁷² and Ser¹⁷³, respectively. The Fab_{OBF} heavy chain also establishes two contact points on CD20_B, one with Tyr¹⁶¹(ECL2b) that packs against Ser³⁰(CDR-H1), Tyr³¹(CDR-H1), Gly⁵⁴(CDR-H2), and Asp⁵⁵(CDR-H2) and another with Glu¹⁷⁴, Ser¹⁷⁷, and Pro¹⁷⁸ on the C-terminal end of EH2 that interact extensively with CDR-H3 residues Asp¹⁰², Gly¹⁰³, and Tyr¹⁰⁴.

The structure of the CD20-Fab_{OBF} complex demonstrates that bound Fab_{OBF} precludes binding of a second molecule on the surface of CD20, because it interacts with the ¹⁷⁴EKN¹⁷⁸ motif in both CD20_A and CD20_B and would generate extensive steric clashes with a second symmetrical Fab_{OBF} molecule, rotated around the pseudo two-fold symmetry axis of CD20. These structures provide the structural basis underlying the differential binding stoichiometry of OBF and in general type II mAbs, compared to type I.

entry of OBF and in general type II mAbs, compared to type I.

Discussion

Our structural and thermodynamic analyses unravel the differential binding mechanisms of major therapeutic anti-CD20 antibodies used in the clinic for the treatment of lymphomas and autoimmune diseases.

The CD20 oligomeric state is important to the mAb binding mechanisms, and we provide strong experimental evidence that the dimer represents a native oligomeric state: the structure of CD20-Fab_{OFA} demonstrated that the CD20 dimer is stabilized by extensive intersubunit contacts that are conserved in the absence of both extensive Fab-Fab homotypic interactions and binding of a single Fab molecule to two CD20 subunits (Fig. 3B). Moreover, in our structures, we observed cholesterol-like lipids bound to the outer and inner halves of the intersubunit interface in a bilayer-like arrangement (Fig. 3A), suggesting that cellular cholesterol further stabilizes the CD20 dimer.

Finally, purified dimeric CD20 both in detergent solution and in lipid membrane recapitulates well the signature properties of type I and type II mAbs observed in B cells.

RTX, OFA, and OBF bind extensive 3D epitopes that extend beyond the core ¹⁷⁰ANPSEKNSP¹⁷⁸ motif. Notably, Fab_{RTX} (22) and Fab_{OBF} (23) bind CD20 cyclic peptides encompassing this motif with similar coordination as in the cryo-EM structures, but with nearly three orders of magnitude weaker affinity (23) compared to full-length CD20 (table S1). This difference highlights the importance of the epitopic expansion observed in the cryo-EM structures and predicts that secondary epitopes outside the above-mentioned motif contribute ~30% to the total mAb binding energy. Moreover, there is ~1 kcal excess binding energy of RTX, over that of OBF and OFA, arguing that the homotypic interface contributes weakly (~10%) to that energy, due to the entropic penalty associated with tightly packing two Fab molecules. However, this interface might play a significant kinetic role by slowing down RTX

dissociation from CD20. The crystal structure of ocrelizumab (OCR) Fab—a murine type I mAb approved for multiple sclerosis treatment (30)—in complex with CD20 peptide (31) shows a Fab-Fab interface within the crystal lattice nearly identical to that of RTX (fig. S8B), suggesting that Fab_{OCR} molecules bound to full-length CD20 also form extensive homotypic interactions.

The key mechanistic difference between IgG type I (IgG_I) and type II (IgG_{II}) molecules is that upon binding to CD20, IgG_{II} forms 1:2 (IgG_{II}:CD20) “terminal” complexes that preclude binding of additional IgG_{II} molecules, while IgG_I forms 1:2 or 2:1 (IgG_I:CD20) “seeding” complexes that enable subsequent concatenation of IgG or CD20 molecules, respectively (Fig. 5A). Hence, seeding and terminal complexes explain the half-maximal saturation values of IgG_{II} compared to IgG_I reported in cells (6).

Both IgG_I and IgG_{II} are able to recruit complement to similar levels, although IgG_I does so with half-saturation values 10- to 1000-fold lower than IgG_{II}, depending on whether CD20 expression levels are high (~10⁶ copies per cell) or low (~10⁴ copies per cell), respectively (32). Indeed, concatenation of IgG_I molecules upon binding to CD20 would increase locally the concentration of Fc domains and promote their oligomerization for C1q recruitment. In turn, IgG_{II} terminal complexes—unable to concatenate additional molecules—would require higher antigen densities for Fc oligomerization, explaining why the difference in IgG_I and IgG_{II} complement recruitment potency strongly depends on CD20 expression levels.

The above arguments raise the important question of why OFA activates complement more potently than RTX, considering that both are able to form seeding complexes. The sharper binding angle of Fab_{OFA} compared to Fab_{RTX} suggests that concatenation of IgG_{OFA} seeding complexes would bring their Fc domains in closer proximity, further facilitating their oligomerization. To visualize this effect, we built symmetrical and circular arrangements of six CD20-Fab_{RTX} and CD20-Fab_{OFA} copies, respectively, around a hexameric Fc ring as the one required for optimal complex

recruitment (9, 11, 33) (Fig. 5B). This speculative model showed that CD20-bound Fab_{OFA} molecules localize ~15 Å closer to the corresponding Fc domain than Fab_{RTX}, supporting the idea that concatenation of CD20-IgG_{OFA} complexes upon binding to CD20 in the membrane forms more compact assemblies and brings Fc in closer proximity for oligomerization. Finally, it is also likely that the lack of homotypic interactions between bound Fab_{OFA} molecules confers a higher degree of freedom to the 2:1 seeding complexes for further facilitation of Fc oligomerization. From all the above, we conclude that IgG binding stoichiometry is a key determinant of the mAb potency to recruit complement, but the angle and flexibility of CD20-bound Fab molecules in seeding complexes also contribute to it.

The molecular mechanisms presented here should facilitate the rational design of new generations of mAbs and biosimilar molecules to fine-tune treatments of different B cell malignancies and autoimmune diseases, as well as to make these more affordable to health care systems.

REFERENCES AND NOTES

1. K. Ishibashi, M. Suzuki, S. Sasaki, M. Imai, *Gene* **264**, 87–93 (2001).
2. Y. Liang, T. F. Tedder, *Genomics* **72**, 119–127 (2001).
3. D. A. Einfeld, J. P. Brown, M. A. Valentine, E. A. Clark, J. A. Ledbetter, *EMBO J.* **7**, 711–717 (1988).
4. R. J. Petrie, J. P. Deans, *J. Immunol.* **169**, 2886–2891 (2002).
5. J. P. Deans, S. M. Robbins, M. J. Polyak, J. A. Savage, *J. Biol. Chem.* **273**, 344–348 (1998).
6. M. S. Cragg *et al.*, *Blood* **101**, 1045–1052 (2003).
7. M. S. Cragg, M. J. Glennie, *Blood* **103**, 2738–2743 (2004).
8. M. J. E. Marshall, R. J. Stopforth, M. S. Cragg, *Front. Immunol.* **8**, 1245 (2017).
9. C. A. Diebold *et al.*, *Science* **343**, 1260–1263 (2014).
10. G. Wang *et al.*, *Mol. Cell* **63**, 135–145 (2016).
11. D. Ugurlar *et al.*, *Science* **359**, 794–797 (2018).
12. T. M. Pierpont, C. B. Limper, K. L. Richards, *Front. Oncol.* **8**, 163 (2018).
13. F. H. Du, E. A. Mills, Y. Mao-Draayer, *Auto Immun. Highlights* **8**, 12 (2017).
14. D. G. Maloney *et al.*, *Blood* **84**, 2457–2466 (1994).
15. E. Mössner *et al.*, *Blood* **115**, 4393–4402 (2010).
16. J. L. Teeling *et al.*, *Blood* **104**, 1793–1800 (2004).
17. G. Cartron, H. Watier, *Blood* **130**, 581–589 (2017).
18. A. W. Pawluczko *et al.*, *J. Immunol.* **183**, 749–758 (2009).
19. S. O'Brien, A. Osterborg, *Clin. Lymphoma Myeloma Leuk.* **10**, 361–368 (2010).
20. M. J. Polyak, J. P. Deans, *Blood* **99**, 3256–3262 (2002).
21. M. Binder, F. Otto, R. Mertelsmann, H. Veelken, M. Trepel, *Blood* **108**, 1975–1978 (2006).

22. J. Du *et al.*, *J. Biol. Chem.* **282**, 15073–15080 (2007).
23. G. Niederfellner *et al.*, *Blood* **118**, 358–367 (2011).
24. C. Klein *et al.*, *mAbs* **5**, 22–33 (2013).
25. L. Rougé *et al.*, *Science* **367**, 1224–1230 (2020).
26. T. Wiseman, S. Williston, J. F. Brandts, L. N. Lin, *Anal. Biochem.* **179**, 131–137 (1989).
27. D. Burnouf *et al.*, *J. Am. Chem. Soc.* **134**, 559–565 (2012).
28. J. L. Teeling *et al.*, *J. Immunol.* **177**, 362–371 (2006).
29. A. Horovitz, *Fold. Des.* **1**, R121–R126 (1996).
30. S. Faissner, J. R. Plemel, R. Gold, V. W. Yong, *Nat. Rev. Drug Discov.* **18**, 905–922 (2019).
31. J. Du *et al.*, *Mol. Immunol.* **45**, 2861–2868 (2008).
32. S. Herter *et al.*, *Mol. Cancer Ther.* **12**, 2031–2042 (2013).
33. Y. Wu *et al.*, *Cell Rep.* **5**, 1443–1455 (2013).

ACKNOWLEDGMENTS

We thank P. V. Krasteva (IECB, Bordeaux) for help with negative-stained EM imaging and discussion; J. Prigent and A. Kok (Humoral Immunology Lab) for help with production of recombinant antibodies and fragments; and C. Velours (I2BC, Paris-Saclay) for SEC-MALS analysis. We acknowledge the IECB cryo-EM imaging facility for support in cryo-EM sample screening and initial data acquisition, the EMBL-Heidelberg Cryo-Electron Microscopy Service Platform for support in image acquisition of CD20-Fab_{RTX} and CD20-Fab_{OFA} complexes, and the Institut Pasteur cryo-EM Nanoimaging Facility for image acquisition of the CD20-Fab_{OFA} complex. **Funding:** This research was supported by ERC Grant 309657 and Institut Pasteur funds to N.R.; CNRS funds to N.R. and R.F.; G5 Institut Pasteur, *Milieu Interieur* (ANR-10-LABX-69-01) Programs, and INSERM funds to H.M. Anand Kumar was supported by fellowships from the Pasteur-Paris University (PPU) international PhD program and Fondation-ARC. CACSICE grant (ANR-11-EQPX-008) supported access to the Institut Pasteur cryo-EM Nanoimaging Facility. **Author contributions:** A.K. optimized and performed protein expression, purification, cryo-EM sample preparation, and functional assays; C.P. and H.M. cloned CD20 and anti-CD20 molecules and produced and purified recombinant antibodies and fragments. A.K. collected cryo-EM data, and A.K., R.F., and N.R. analyzed cryo-EM data. A.K. and N.R. built structural models, analyzed structures, and prepared the manuscript with comments and edits from R.F. and H.M.; N.R. conceived and supervised the project. **Competing interests:** The authors declare no competing interests. **Data and materials availability:** Structural models of CD20-Fab_{RTX}, CD20-Fab_{OFA}, CD20-Fab_{OFA}, and CD20-Fv_{OFA} have been deposited in Protein Data Bank (PDB) with accession codes 6Y90, 6Y92, 6Y97, and 6Y9A, respectively. The corresponding cryo-EM maps were deposited in the Electron Microscopy Data Bank (EMDB) under accession numbers EMD-10731, EMD-10732, EMD-10733, and EMD-10734. All data are available in the main text or the supplementary materials. Materials are available upon reasonable request.

SUPPLEMENTARY MATERIALS

science.sciencemag.org/content/369/6505/793/suppl/DC1
Materials and Methods
Figs. S1 to S8
Tables S1 to S5
References (34–44)
MDAR Reproducibility Checklist

[View/request a protocol for this paper from Bio-protocol.](#)

19 March 2020; accepted 22 June 2020
10.1126/science.abb8008